

Weakly spin-dependent band structures of antiferromagnetic perovskite LaMO_3 ($\text{M} = \text{Cr, Mn, Fe}$)

Takuya Okugawa,¹ Kaoru Ohno,^{1,2} Yusuke Noda,³ and Shinichiro Nakamura²

¹*Department of Physics, Yokohama National University,
79-5 Tokiwadai, Hogogaya-ku, Yokohama 240-8501, Japan*

²*RIKEN Innovation Center, Nakamura Laboratory,
2-1 Hirosawa, Wako, Saitama 351-0198, Japan*

³*Center for Materials Research by Information Integration (CMI²),
Research and Services Division of Materials Data and Integrated System (MaDIS),
National Institute for Materials Science (NIMS),
1-2-1 Sengen, Tsukuba, Ibaraki 305-0047, Japan*

(Dated: October 16, 2017)

Abstract

We investigate spin-dependent electronic states of antiferromagnetic (AFM) lanthanum chromite (LaCrO_3), lanthanum manganite (LaMnO_3), and lanthanum ferrite (LaFeO_3) using spin-polarized first-principles density functional theory (DFT) with Hubbard U correction. The band structures are calculated for 15 types of their different AFM structures. It is verified for these structures that there is a very simple rule to identify which wave number \mathbf{k} exhibits spin splitting or degeneracy in the band structure. This rule uses the symmetry operations that map the up-spin atoms onto the down-spin atoms. The resulting spin splitting is very small for the most stable spin configuration of the most stable experimental structure. We discuss a plausible benefit of this characteristic, *i.e.*, the direction-independence of the spin current, in electrode applications.

This paper was published in Ref. [57]:

Takuya Okugawa, Kaoru Ohno, Yusuke Noda, and Shinichiro Nakamura, “Weakly spin-dependent band structures of antiferromagnetic perovskite LaMO_3 ($\text{M} = \text{Cr, Mn, Fe}$)”, Journal of Physics: Condensed Matter **30**, 075502 (2018). DOI: 10.1088/1361-648X/aa9e70

I. INTRODUCTION

Materials with perovskite-like structures have many interesting properties such as ferroelectricity¹, superconductivity², photovoltaics³, catalytic behaviours for the oxygen evolving reaction (OER) or the oxygen reduction reaction (ORR)^{4–6}, spin-dependent transport⁷, and colossal magnetoresistance (CMR)^{8–10}; $\text{La}_{0.67}\text{Ca}_{0.33}\text{MnO}_x$ exhibits a huge negative magnetic resistance called the CMR^{8–10}, which is applied to magnetic field sensors for reading and writing data in hard disks. The formal valence state of $\text{La}_{1-x}\text{Ca}_x\text{MnO}_3$ is $\text{La}^{3+}\text{Mn}^{3+}\text{O}_3^{2-}$ for $x = 0$ and $\text{Ca}^{2+}\text{Mn}^{4+}\text{O}_3^{2-}$ for $x = 1$; it becomes a mixed valence state of Mn^{3+} and Mn^{4+} for $x \sim 1/3$, and, in this case, the ferromagnetic (FM) coupling is favored due to the double exchange mechanism as explained by Goodenough¹¹ and Coey *et al.*¹⁰. Then, just below the Curie temperature, due to the huge magnetic fluctuations, spin current is significantly scattered, and the electric resistance is high. However, the applied magnetic field can line up the magnetic orderings, leading to the significant reduction of the electric resistance.

Not only these complex materials but also its mother material, lanthanum manganite (III) (LaMnO_3), has been investigated in detail, and it is now well known that LaMnO_3 has a strongly distorted structure^{12,13}, and shows so-called A-type antiferromagnetic (AFM) ordering below the Néel temperature^{12,14,15}. Similarly, lanthanum chromite (LaCrO_3) and lanthanum ferrite (LaFeO_3) have the same structure as LaMnO_3 ^{15–19} and they exhibit so-called G-type AFM ordering below the Néel temperature¹⁵. The OER and ORR of these perovskite materials have been investigated more recently as an application to electrodes^{4–6}. For these electrochemical reactions, the surface geometry and the surface state related to $\text{Cr}^{2+}/\text{Cr}^{3+}/\text{Cr}^{4+}$, $\text{Mn}^{2+}/\text{Mn}^{3+}/\text{Mn}^{4+}$, and $\text{Fe}^{2+}/\text{Fe}^{3+}$ play an essential role. So far, many theoretical calculations using density functional theory (DFT)^{20–35} as well as mapping onto tight-binding or spin models^{36–38} have been performed for these materials. Despite these many theoretical studies, there has been only little systematic comparison of all possible structures of AFM perovskite LaMO_3 ($\text{M} = \text{Cr, Mn, Fe}$) to find out the similarities and differences among them in particular in the spin-dependent feature of the electronic states.

There is a naive consensus that, if magnetic ions occupy crystallographically equivalent sites, the band structures of the up- and down-spin states in antiferromagnetic materials should be the same. However, is it really true? This question reminds us at least two fundamentally important facts.

One is the fact related to the spontaneous symmetry breaking in infinite systems. For infinite size antiferromagnetic materials, the magnetic symmetry is broken below the Néel temperature. Then, even if all magnetic ions occupy crystallographically equivalent lattice sites, there appears a clear distinction in the lattice sites of the up- and down-spin ions, and the positions of their net components are spatially fixed in a alternating way inside the magnetic domain, although there are of course thermal and quantum fluctuations. That is, it becomes impossible to reverse all spins in a huge single magnetic domain at once because it requires a huge energy. This is similar to the situation of a ferromagnetic phase transition; the only difference is that the lattice is divided into the up-spin A sublattice and the down-spin B sublattice in an antiferromagnetic case. Then, the crystal symmetry is lowered to a new symmetry, which is identical to the symmetry of either the up-spin A sublattice or the down-spin B sublattice; if the A sublattice symmetry is different from the B sublattice symmetry, the lower symmetry is selected. In other words, the symmetry coincides with that of a hypothetical crystal having different atomic species, A and B, respectively, at the A sublattice points and the B sublattice points. Although X-ray diffraction cannot distinguish these up- and down-spin sites, neutron diffraction can clearly distinguish them; the pattern of the diffraction spots change at the Néel temperature to those with the double spatial periodicity. However, one should remark that the spontaneous symmetry breaking, *i.e.*, the phase transition never happens for finite size antiferromagnetic materials. For finite systems, up- and down-spins change in time and no such phase transition takes place.

The other fact is related to the crystal symmetry. When crystallographically equivalent magnetic up- and down-spin ions are aligned alternately in an antiferromagnetic phase, their atomic positions can be interchanged, *i.e.*, they move onto the other sites by a symmetry operation. In real space, applying a symmetry operation is equivalent to changing the view point or the view angle. For example, if the operation is a simple translation, it is clear that the electronic structures of the up-spin and down-spin electrons are the same everywhere in the Brillouin zone because they are not affected by the choice of the origin of the real space coordinate system. However, if the operation R is a two-fold rotation, the electronic structures of the up-spin and down-spin electrons should be interchanged by the same two-fold rotation R ($= R^{-1}$) in the reciprocal space. That is, the electronic band structure at the \mathbf{k} point should be the same as that of the $R\mathbf{k}$ ($= R^{-1}\mathbf{k}$) point. This is the ingredient of our theory.

In either case of the OER and ORR, the spin current in host materials under a carrier doping, *i.e.*, under a certain shift of the chemical potential, plays an essential role in electrodes. In our previous study on various AFM MnO_2 phases³⁹, we demonstrated that the spin current may have spin-dependent preferable directions according to the spin-splitting band structures and that, only for the λ phase, all bands are fully degenerate against spin and no such preferable direction exists in the spin current. In the λ phase, both up- and down-spin currents can coexist in the same direction. On the other hand, in the α , β , and δ phases, there is a spin splitting at the valence band maximum (VBM) and at the conduction band minimum (CBM), only up- or down-spin can contribute to the spin current in one direction. Therefore, fully degenerate bands against spin in AFM phases must be a favourable factor to enhance the OER and ORR activities; in fact, in a recent experiment⁴⁰, the OER activity is higher in the λ phase than the other MnO_2 phases. In this respect, it is worth investigating the amount of spin splitting in the band structure of various AFM perovskite LaMO_3 materials also.

Similarly, it is interesting to consider what happens when the band structure is significantly spin-dependent. Thanks to de Broglie relationship ($\mathbf{p} = \hbar\mathbf{k}$), the direction dependence of the wave vector \mathbf{k} is identical to that of the momentum \mathbf{p} . Then, the property that spin splitting and degeneracy depend on the direction of the wave vector \mathbf{k} may be utilized for spin-dependent carrier transport or spin selection. If the VBM or CBM at the wave vector \mathbf{k} is only composed of up-spin (down-spin) level, the transport phenomena will be mainly governed by the up-spin (down-spin) carrier with the momentum $\hbar\mathbf{k}$. Therefore, spin current has preferable directions in the crystal, and this property may be used for several purposes. For example, the electrons with different spins could be separated by using the direction-dependent spin current in electron- or hole-doped materials.

That is, if the spin-dependance is found in the vicinity of the CBM or VBM, one may consider an application of the materials to new spin-control technology or invent a new spin-device. On the other hand, if the CBM and VBM are both spin degenerate, the materials are considered to be favourable for the OER or ORR in a sense that there is no directional preference in the spin current inside the electrodes. Therefore, not only from purely academic interest but also from practical interest, it is quite desirable to investigate the electronic state of AFM LaMO_3 in terms of spin-dependent features.

In this paper, we study the spin-dependent band structures of LaCrO_3 , LaMnO_3 , and

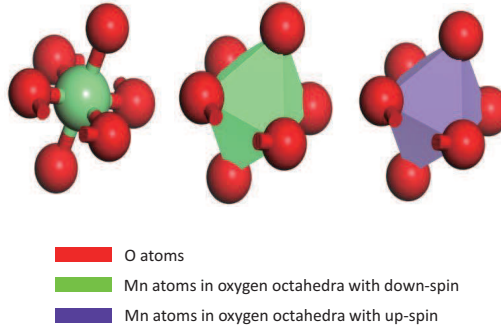


FIG. 1. Oxygen octahedra surrounding Mn atom.

LaFeO₃ using spin-polarized DFT with Hubbard U correction. In section II, we survey the possible structures and spin configurations of LaMO₃. The computational method adopted in this work is explained in detail in section III. Sections IV. A and B are devoted, respectively, to the discussion of the resulting optimized structures and magnetic states and to the general discussion of the spin degeneracy and splitting in energy band diagrams. Then, sections IV. C, D, and E describe the results of A-type, C-type, and G-type experimental structures. We explicitly discuss \mathbf{k} -dependent spin splitting and degeneracy for each structure. The results for less stable structures of LaMO₃ are given in Supplementary Data (SD). In section IV. F, we briefly comment on a preference of the resulting band structures for electrodes. Finally, section V concludes this paper.

II. STRUCTURES AND MAGNETIC CONFIGURATIONS OF LaMO₃ (M = Cr, Mn, Fe)

The strongly distorted structure of LaMO₃ (with $Pbnm$ space group)^{12,13} is derived from the ideal cubic perovskite structure (with $Pm\bar{3}m$ space group) by deformations through an intermediate structure that has a pure Jahn-Teller (JT) distortion only (with $P4/mbm$ space group)^{37,38}. For example, in LaMnO₃, an oxygen octahedron surrounds a Mn atom; see Fig. 1. In what follows, we extensively use this octahedron for the purpose of explaining spin splitting and degeneracy. In Fig. 1, red-coloured balls are O atoms, while green-coloured and magenta-coloured octahedra (a green-coloured ball in the leftmost figure) denote Mn atoms with down- and up-spin, respectively. More details of the structures are explained

below.

First of all, three types of the distinct structures^{37,38} are schematically illustrated in Fig. 2 and explained as follows:

- (1) The ideal cubic perovskite structure, in which all the oxygen octahedra having the same size. Here we allowed a common elongation or shrink in z direction of oxygen tetrahedra, so the resulting actual symmetry may become tetragonal (see also SD).
- (2) The purely JT-distorted structure obtained by alternating long and short O-Mn-O distances in xy -plane from the ideal cubic perovskite structure. If the O-Mn-O distance along x -axis (y -axis) in one oxygen octahedron is longer (shorter), that in adjacent octahedra in the same xy -plane is shorter (longer). Thus, mutually 90 degree rotated (JT-distorted) octahedra are lined up in a checkerboard form. The resulting symmetry is totally tetragonal.
- (3) The experimental structure realized by rotating oxygen octahedra along z -axis and tilting away from z -axis. In addition, lanthanum cations are displaced from their ideal positions within xy -plane. The final symmetry is orthorhombic.

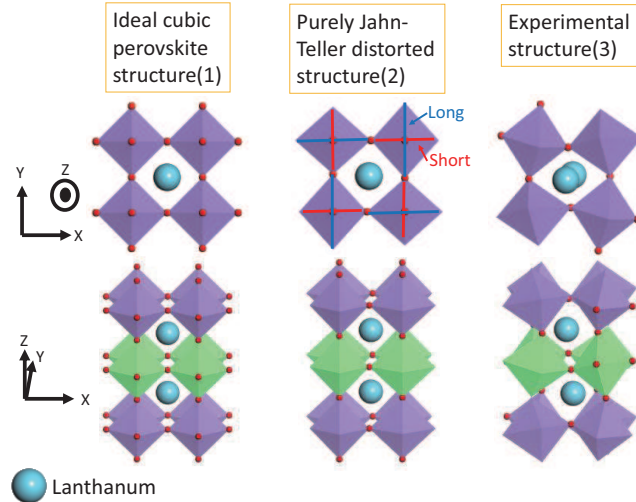


FIG. 2. Three types of distinct structures studied in this work; see also Supplementary Data (SD).

Furthermore, three different magnetic configurations called A-, C- and G-types proposed for LaMnO₃ by Goodenough¹¹ (see also Hotta *et al.*³⁶) are considered in our study also.

Figure 3 shows these three types of magnetic configuration in the case of the ideal cubic perovskite structure.

- (i) A-type antiferromagnetic (A-AFM) configuration having a layer-like structure. Mn atoms inside oxygen octahedra have all up-spin in the first layer, all down-spin in the second layer, and again all up-spin in the third layer.
- (ii) C-type antiferromagnetic (C-AFM) configuration having an alternating spin alignments in xy -plane. The spin directions of all Mn atoms are the same along z -axis, but in xy -plane the neighboring Mn atoms have different spin directions.
- (iii) G-type antiferromagnetic (G-AFM) configuration having an alternating spin alignment in all directions. The neighboring Mn atoms always have different spin directions.

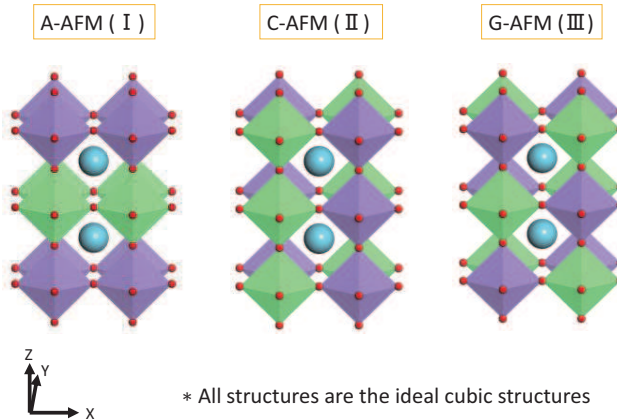


FIG. 3. Three different magnetic configurations, A-AFM, C-AFM, and G-AFM.

Therefore, $3 \times 3 = 9$ types of different LaMnO_3 structures can be considered and each type of LaMnO_3 is expected to show distinct electronic states. In addition, we investigate LaCrO_3 and LaFeO_3 in the case of A-, C-, and G-types AFM experimental (optimized) structures. Thus, the calculations are carried out for $9 + 3 + 3 = 15$ types of structures. All the results except for the experimental structure are presented in Supplementary Data (SD). Also the results for less stable A- and C-type AFM LaFeO_3 and LaCrO_3 are presented in SD.

III. COMPUTATIONAL METHOD

In this study, we use CASTEP program⁴¹⁻⁴³ in the Materials Studio package and perform spin-polarized first-principles DFT calculations using the on-the-fly generation ultra-soft pseudopotential approach⁴⁴. For the exchange-correlation functional, Perdew-Burke-Ernzerhof (PBE) generalized gradient approximation (GGA)⁴⁵ with Hubbard U correction^{46,47} ($U = 2.5$ eV for Mn, Fe, and Cr and 6.0 eV for La) is used. Moreover, the calculations with different values of Hubbard U parameters (1.5 and 3.5 eV for Mn, 5.0 and 7.0 eV for La) are carried out in the case of the A-AFM experimental LaMnO₃ (see Appendix of SD). Even if any of these U parameters are chosen, our discussion on the spin-dependent band structure does not change. Before band calculations, geometrical optimizations were performed together with the unit-cell relaxation. The cutoff energy for plane-wave basis is set at 571.4 eV for all our calculations. To get converged results, we set Gaussian smearing at 0.15 eV for geometrical optimization and 0.01 eV for the band calculation. The initial magnetic moment of M is set at $\pm 5.00\mu_B$.

For \mathbf{k} -points, we employ Monkhorst-Pack grids⁴⁸ of $6\times 6\times 3$, $4\times 4\times 6$, and $4\times 4\times 4$ for the A-, C-, and G-AFM ideal cubic perovskite structures, respectively. Also we use \mathbf{k} -point grids of $4\times 4\times 3$, $3\times 3\times 6$, and $4\times 4\times 6$ for the A-, C-, and G-AFM purely Jahn-Teller distorted structures, respectively. Finally, for all magnetic configurations of the experimental structure, the $4\times 4\times 3$ grid is used.

All these set of parameters are required to get good convergence of the results.

IV. RESULTS AND DISCUSSION

A. Optimized structures and magnetic states

First of all, we summarize the space group and lattice constants obtained by geometrical optimizations together with the corresponding experimental data (written in parentheses) for the most stable experimental structure in Table I. The estimated total energy of these structures are listed in Table II. (For the less stable ideal cubic and JT-distorted structures of LaMO₃ (M = Cr, Mn, Fe) as well as the A- and C-AFM experimental structures of LaCrO₃ and LaFeO₃, see SD.) From this table, it is found that LaCrO₃, LaMnO₃, and LaFeO₃

TABLE I. Space group and lattice constants (a, b, c) for three spin configurations (Spin config.) of the most stable experimental structure (Exp. struct.). Values inside parentheses are experimental data^{12,18}. All other values are calculated by structural optimizations.

Exp. struct.	Spin config.	Space group	Lattice constants (Å)		
			a	b	c
	A-AFM	$P2_1/c$	5.584	5.616	7.892
LaCrO ₃	C-AFM	$P2_1/m$	5.587	5.594	7.902
<i>Pbnm</i>	G-AFM	$P2_1/c$	5.595 (5.479) ^a	5.573 (5.513) ^a	7.881 (7.759) ^a
	A-AFM	$P2_1/c$	5.635 (5.532) ^b	5.886 (5.742) ^b	7.774 (7.668) ^b
LaMnO ₃	<i>Pbnm</i>	C-AFM $P2_1/m$	5.599	6.060	7.735
	G-AFM	$P2_1/c$	5.596	6.137	7.679
	A-AFM	$P2_1/c$	5.631	5.732	7.953
LaFeO ₃	C-AFM	$P2_1/m$	5.617	5.685	7.998
<i>Pbnm</i>	G-AFM	$P2_1/c$	5.611 (5.553) ^a	5.689 (5.563) ^a	7.970 (7.857) ^a

^a Ref.¹⁸.

^b Ref.¹².

TABLE II. Total energy difference relative to the most stable spin configuration (A-AFM for LaMnO₃ and G-AFM for LaCrO₃ and LaFeO₃) of the most stable experimental structure in units of eV.

Experimental structure	Relative energy (eV)		
	A-AFM	C-AFM	G-AFM
LaCrO ₃	0.151	0.069	0.000
LaMnO ₃	0.000	0.237	0.269
LaFeO ₃	0.853	0.378	0.000

prefer G-AFM, A-AFM, and G-AFM, respectively, in accordance with the experimental evidence^{12,14,15}. The calculated band gaps of the most stable experimental structures are given in Table III together with the experimental values^{49–53}.

TABLE III. Energy band gap of the most stable experimental structures. Values inside parentheses are experimental data^{49–53}. All other values are calculated results.

Experimental structure	Band gap (eV)		
	A-AFM	C-AFM	G-AFM
LaCrO ₃	1.399	1.604	2.125 (2.8 ^a)
LaMnO ₃	0.647 (0.24 ^b , 1.2 ^c)	0.654	1.278
LaFeO ₃	0.120	0.943	1.584 (2.1 ^d , 2.4 ^e)

^a Ref.⁴⁹.

^b Ref.⁵⁰.

^c Ref.⁵¹.

^d Ref.⁵².

^e Ref.⁵³.

If we ignore the magnetic spin configuration, the space-group symmetry of the experimental structure is $Pbnm$ or equivalently D_{2h} , which has 8 symmetry operations including three 180 degree rotations around x , y , and z axis, respectively, with translations in [110], [111] and [001] directions: $T[110]C_2^x$, $T[111]C_2^y$, $T[001]C_2^z$. However, due to the regular AFM alignment of the electron spins, the real symmetry is lowered to $P2_1/c$ for A-AFM and G-AFM, and $P2_1/m$ for C-AFM (see Table I), which are equivalent to C_{2v} having 4 symmetry operations including only one 180 degree rotation. Therefore, A-AFM, C-AFM, and G-AFM have, respectively, $T[110]C_2^x$, $T[001]C_2^z$, and $T[111]C_2^y$ (180 degree rotation) only. In what follows, we will extensively discuss the rest two 180 degree rotations, *i.e.*, $T[111]C_2^y$ and $T[001]C_2^z$ in A-AFM, $T[110]C_2^x$, $T[111]C_2^y$ in C-AFM, and $T[110]C_2^x$ and $T[001]C_2^z$ in G-AFM, which are missing in the lower $P2_1/c$ or $P2_1/m$ symmetry with spin distinction but existing in the higher $Pbnm$ symmetry without spin distinction. These two 180 degree rotations in each spin configuration map the up-spin atoms onto the down-spin atoms.

For the most stable structure with the most stable magnetic configuration, Table IV lists the spin magnetic moment of M, the Hirshfeld charge⁵⁴ of La and M (normalized to give -2.0 for O^{2-}), and M-O-M angles; note that there are two different angles M-O1-M (in z direction) and M-O2-M (in xy -plane), because z direction is elongated or shrunk compared

to x and y directions. The z coordinate of O1 (O2) is almost the same as that of La (M). The spin magnetic moments for $M = Cr, Mn$, and Fe are very roughly $3\mu_B$, $4\mu_B$, and $4(\sim 5)\mu_B$, respectively, almost corresponding to the trivalent ionicity (M^{3+}), although there is some deviation in Fe . The trivalent ionicities $Cr(III)$, $Mn(III)$, and $Fe(III)$ are consistent with the calculated results for the Hirshfeld charge; 3.2, 2.4, and 2.7, respectively, for Cr , Mn , and Fe , as shown in Table IV. In the same way, we also very roughly identify the valence ionicity of La to be 3 from the Hirshfeld charge; 2.4, 3.1, and 2.9 for La of $LaCrO_3$, $LaMnO_3$, and $LaFeO_3$, respectively. The $M-O1/O2-M$ angles are all between 90° and 180° , and would rather closer to 180° . According to the theory of Kanamori⁵⁵ on the superexchange interaction (see also Goodenough¹¹), two adjacent $3d$ (M) atoms favour antiparallel (parallel) spin alignment when the $M-O-M$ angle equals to 180° (90°). Therefore, the G-type AFM spin configuration might be generally considered to be more stable than the A-type and C-type spin configurations. Indeed, the G-type AFM configuration, which is fully AFM in all directions is realized in $LaCrO_3$ and $LaFeO_3$. However, for $LaMnO_3$, the A-type AFM configuration, which is AFM in z direction and FM in xy -plane, is energetically more favourable and realized in nature. Concerning this discrepancy, one may remark the fact that the lattice constant a ($\simeq b$) to c ratio is close to the ideal value $\sqrt{2}$ for $LaCrO_3$ and $LaFeO_3$ but somewhat smaller than the ideal value (~ 1.35) for $LaMnO_3$ as seen in Table I. The larger (shorter) interatomic distance in xy -plane (in z direction) keeping the $M-O1/O2-M$ angles, *i.e.* the Jahn-Teller distortion of the octahedra, is the reason of favouring the A-type AFM of $LaMnO_3$. A possible explanation on this difference is that two e_g levels are empty in Cr^{3+} and fully occupied by the majority spin in Fe^{3+} , but only one of the two e_g levels is occupied by the majority spin in Mn^{3+} . Since the half filling of the e_g state is similar to the mixed valence (Mn^{3+} and Mn^{4+}) systems, there is a double exchange interaction favouring the FM coupling that competes with the superexchange interaction favouring the AFM coupling, resulting in the A-type AFM due to the Jahn-Teller distortion of $LaMnO_3$ ^{20,24,56}. From Table II, however, we see that the total energy differences among A-, C-, and G-types of $LaMnO_3$ ($LaCrO_3$) are less than 0.27 eV (0.16 eV), suggesting that the mechanism favouring these special spin configurations is related to a very subtle energy balance. We do not go into further detail because the main purpose of this paper is not to discuss the origin of magnetic interactions but to discuss the spin degeneracy and splitting of the resulting electronic band structures.

TABLE IV. Calculated and experimental spin magnetic moments of M (M = Cr, Mn, and Fe), the Hirshfeld charge⁵⁴ of La and M (normalized to give -2.0 for O^{2-}), and M-O1/O2-M angles, for the most stable structure with the most stable magnetic configuration. The z coordinates of O1 and O2 are almost the same as those of La and M, respectively. Available experimental data^{12,13,15,16,19} are also listed for comparison.

Exp.	Magnetic moment of M (μ_B)		Hirshfeld charge		M-O1-M angle ($^\circ$)		M-O2-M angle ($^\circ$)		
	struct.	calc.	exp.	La	M	calc.	exp.	calc.	exp.
LaCrO ₃	2.68		2.8 ± 0.2^a	2.4	3.2	157.58	161.36^b	159.95	161.36^b
LaMnO ₃	3.67		$3.9 \pm 0.2^a, 3.7 \pm 0.1^c$	3.1	2.4	153.15	156.0 ± 0.3^d	154.86	156 ± 1^d
LaFeO ₃	3.81		$4.6 \pm 0.2^a, 3.77^e$	2.9	2.7	155.44	156.8 ^e	155.36	156.8 ^e

^a Ref.¹⁵.

^b Ref.¹⁶.

^c Ref.¹².

^d Ref.¹³.

^e Ref.¹⁹.

B. Spin degeneracy and splitting

Here we explain in detail the very simple rule proposed in the preceding paper³⁹ to identify which wave number \mathbf{k} exhibits spin splitting or degeneracy in the band structure. The Kohn-Sham (or quasiparticle) equations for the up-spin and down-spin electrons are represented as follows:

$$\left[\frac{1}{2}(\mathbf{k} - i\nabla)^2 + V_{\uparrow} \right] u_{\mathbf{k}\uparrow} = \epsilon_{\mathbf{k}\uparrow} u_{\mathbf{k}\uparrow}, \quad (1)$$

$$\left[\frac{1}{2}(\mathbf{k} - i\nabla)^2 + V_{\downarrow} \right] u_{\mathbf{k}\downarrow} = \epsilon_{\mathbf{k}\downarrow} u_{\mathbf{k}\downarrow}, \quad (2)$$

where \mathbf{k} is the wave vector, V_{σ} ($\sigma = \uparrow, \downarrow$) is the effective single-electron potential including the exchange-correlation potential (or the self-energy), $u_{\mathbf{k}\sigma}$ is the periodic part of the eigenfunction, and $\epsilon_{\mathbf{k}\sigma}$ is the eigenvalue at one \mathbf{k} -point.

Now, consider symmetry operations R that belong to the (higher symmetry) space group for the atomic geometry ignoring spin orientations but that do not belong to the (lower symmetry) space group for the spin configuration. They satisfy

$$RV_{\sigma}R^{-1} = V_{-\sigma}, \quad (3)$$

i.e., they map the up-spin atoms onto the down-spin atoms and vice versa. Such symmetry operations, R , map the green-coloured (Mn atom with down-spin) octahedra onto those of magenta-coloured (Mn atom with up-spin); hereafter we will call such operations the exchange operations. Then, for the \mathbf{k} -points exhibiting spin degeneracy, one must find at least one such R that satisfies

$$R\mathbf{k} = \mathbf{k}. \quad (4)$$

Indeed, R that satisfies both Eqs. (3) and (4) transforms the square parentheses, *i.e.* the effective Hamiltonian, of Eq. (1) to that of Eq. (2). Therefore, the eigenvalues of the two equations (1) and (2) must be the same:

$$\epsilon_{\mathbf{k}\uparrow} = \epsilon_{\mathbf{k}\downarrow}. \quad (5)$$

That is, spin degeneracy occurs at those \mathbf{k} -points that do not change (*i.e.*, satisfies Eq. (4)) under at least one of the exchange operations, R .

On the other hand, if there is no R satisfying Eq. (4), those \mathbf{k} -points exhibit spin splitting. In this case, Eq. (4) is replaced by

$$R\mathbf{k} = \mathbf{k}'. \quad (6)$$

Then, R that satisfies both Eqs. (3) and (6) transforms the effective Hamiltonian of Eq. (1) at \mathbf{k} to that of Eq. (2) at \mathbf{k}' . Therefore, the eigenvalue of up-spin electrons at the \mathbf{k} -point and that of down-spin electrons at the \mathbf{k}' -point must be the same:

$$\epsilon_{\mathbf{k}\uparrow} = \epsilon_{\mathbf{k}'\downarrow}. \quad (7)$$

Thus, if Eq. (6) holds for one of the exchange operations, R , at some \mathbf{k} - and \mathbf{k}' -points, the up-spin (down-spin) energy at the \mathbf{k} -points and that of the down-spin (up-spin) at the \mathbf{k}' -points become the same.

This rule is a very general one³⁹, and therefore should be applied to all the systems considered here. In what follows, we discuss spin splitting and degeneracy of the most stable experimental structure in detail. The results and discussion for less stable cubic and JT-distorted structures of LaMnO₃ as well as the A- and C-AFM experimental structures of LaCrO₃ and LaFeO₃ are given in SD.

C. A-type AFM experimental structure

1. $LaMnO_3$

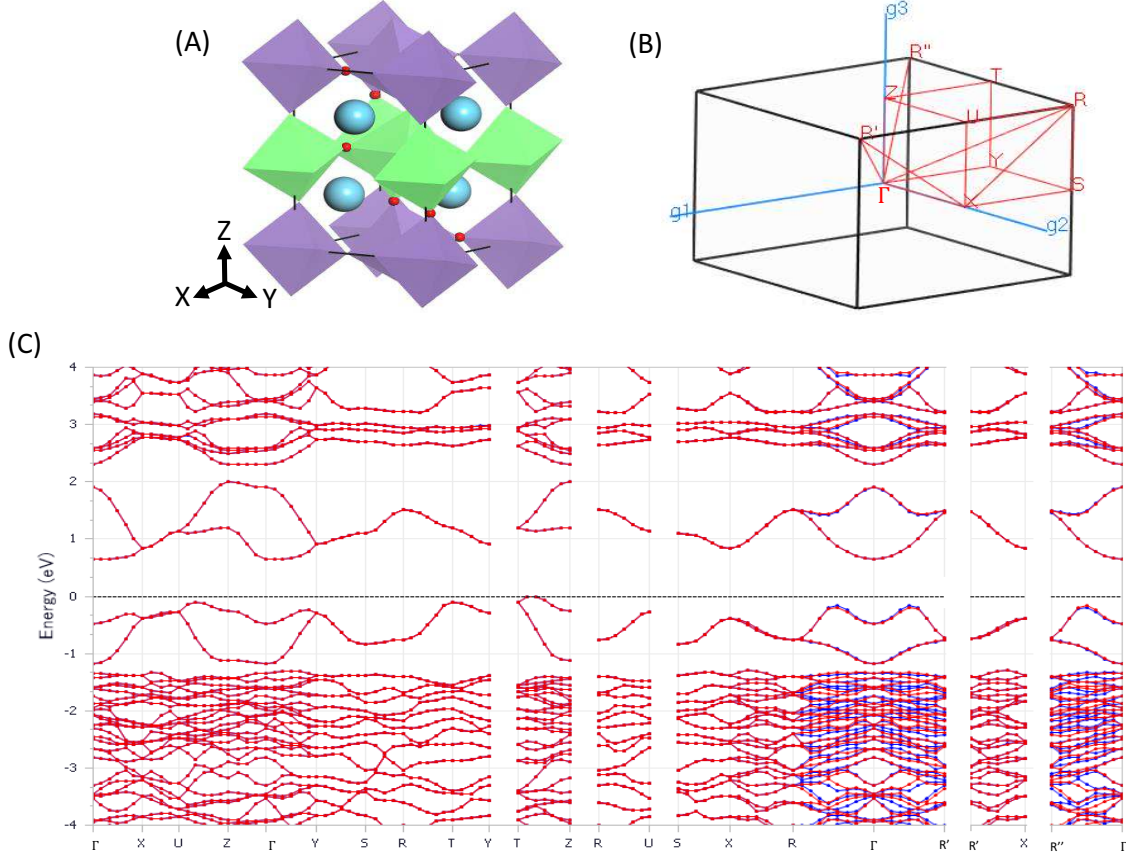


FIG. 4. (A) Unit cell and (B) Brillouin zone of the A-AFM $LaMnO_3$ experimental ORC structure. (C) Resulting band structure, in which red and blue lines denote up- and down-spin electron levels, respectively.

The A-AFM experimental structure is the most stable atomic and spin configuration of $LaFeO_3$, and has a space-group symmetry $Pbnm$ with a simple orthorhombic lattice (ORC, see Fig. 4(A)) if we ignore the spin configuration. This space-group symmetry is lowered to $P2_1/c$ when the spin configuration is taken into account. This structure with this spin configuration is actually observed experimentally^{12,14,15}. The lattice constants inferred from our geometrical optimization are $a = 5.635 \text{ \AA}$, $b = 5.886 \text{ \AA}$, $c = 7.774 \text{ \AA}$ (experimental lattice constants¹² are $a = 5.532 \text{ \AA}$, $b = 5.742 \text{ \AA}$, $c = 7.668 \text{ \AA}$) as shown in Table I. Figure 4(B)

is the Brillouin zone of this structure. The band structure is shown in Fig. 4(C). There is a band gap of amount 0.647 eV, which should be compared with the experimental values 0.24 eV¹⁶ and 1.2 eV¹² as listed in Table III. We added other symmetry \mathbf{k} -lines to those in the conventional Brillouin zone to discuss the spin-dependent band structure. Similar to the A- and G-AFM ideal cubic perovskite structures (see SD), the up- and down-spin energy are completely the same along Γ -X-U-Z- Γ -Y-S-R-T-Y, T-Z, R-U, S-X-R, and R'-X \mathbf{k} -lines. However, unlike their structures, one can see spin splitting along R- Γ -R' and R"- Γ \mathbf{k} -lines. In short, the spin splitting and degeneracy occur depending on \mathbf{k} -points in some manners. It means that there is a momentum dependence in the band spin splitting and degeneracy. We confirmed that different sets of Hubbard U parameters do not change the \mathbf{k} -points exhibiting spin degeneracy and those exhibiting spin splitting (see Appendix of SD). The characteristic of this spin-dependent band structure can be explained according to the rule described in sections IV. B as follows.

2. Spin degeneracy and splitting

Different from the ideal cubic structure (see SD), we cannot find any translations as the exchange operation in any direction. Translations cannot exactly map green-coloured octahedra onto the same structure of magenta-coloured octahedra because these octahedra are distorted, rotated and tilted. However, a combination of 180 degree-rotation C_2 around y -axis and translation along [111] direction can correctly map green-coloured octahedra onto the same structure of magenta-coloured octahedra:

$$TC_2^y V_\downarrow (TC_2^y)^{-1} = V_\uparrow. \quad (8)$$

Under this operation, \mathbf{k} -points on the Γ -X line in the reciprocal lattice space do not change:

$$TC_2^y \mathbf{k} = \mathbf{k} \quad \text{for } \Gamma\text{-X line.} \quad (9)$$

Furthermore, because the Brillouin zone is periodic, \mathbf{k} -points on the Y-S, T-R, and Z-U lines can go back to the original points by adding a reciprocal lattice vector \mathbf{G} if necessary, under the TC_2^y operation:

$$TC_2^y \mathbf{k} = \mathbf{k} + \mathbf{G} \quad \text{for Y-S, T-R, and Z-U lines.} \quad (10)$$

Moreover, inversion I does not change the structure and the spin configuration; green-coloured octahedra are mapped onto those of green-coloured by inversion. Therefore, the combination of 180 degree-rotation around y -axis, translation along [111] direction, and inversion can map green-coloured octahedra onto those of magenta-coloured:

$$ITC_2^y V_{\downarrow} (ITC_2^y)^{-1} = V_{\uparrow}. \quad (11)$$

Under these operations, \mathbf{k} -points on the Γ -Y-T-Z- Γ , X-S-R-U-X, X-R', and X-R lines in the reciprocal lattice space do not change:

$$ITC_2^y \mathbf{k} = \mathbf{k} \quad \text{for } \Gamma\text{-Y-T-Z-}\Gamma \text{ line,} \quad (12)$$

$$ITC_2^y \mathbf{k} = \mathbf{k} + \mathbf{G} \quad \text{for X-S-R-U-X, X-R', and X-R lines.} \quad (13)$$

In addition to this combination, we can find a combination of 180 degree-rotation C_2 around z -axis and translation along [001] direction as the exchange operation. However, the \mathbf{k} -points on the R- Γ -R' and Γ -R" lines do not map onto themselves even with this exchange operation. Thus, we observe spin splitting at such \mathbf{k} -points. Under the former exchange operation (11), \mathbf{k} -points on the Γ -R" symmetry line map onto the \mathbf{k} -points on the Γ -R symmetry line:

$$ITC_2^y \mathbf{k} (\Gamma\text{-R"}) = \mathbf{k} (\Gamma\text{-R}). \quad (14)$$

On the other hand, under the latter exchange interaction made by the combination of the 180 degree-rotation around z -axis and the translation along [001] direction, those \mathbf{k} -points map onto the \mathbf{k} -points on the Γ -R' symmetry line:

$$TC_2^z \mathbf{k} (\Gamma\text{-R"}) = \mathbf{k} (\Gamma\text{-R'}). \quad (15)$$

Therefore, the up-spin (down-spin) energy on the Γ -R" line is the same as the down-spin (up-spin) energy on the Γ -R and Γ -R' lines.

In summary, we find spin degeneracy for all \mathbf{k} -points on the Γ -X-U-Z- Γ -Y-S-R-T-Y, T-Z, R-U, S-X-R, and R'-X lines and spin splitting on the R- Γ -R' and R"- Γ lines.

D. C-type AFM experimental structure

1. $LaMnO_3$

The C-AFM $LaMnO_3$ experimental structure has a space-group symmetry $Pbnm$ with a simple orthorhombic lattice (ORC, see Fig. 5(A)), which is lowered to $P2_1/m$ by taking into

account the spin configuration. The relaxed lattice constants are $a = 5.599 \text{ \AA}$, $b = 6.060 \text{ \AA}$, $c = 7.735 \text{ \AA}$ as shown in Table I. Figure 5(B) is the Brillouin zone of this structure. The band structure is shown in Fig. 5(C). The amount of the band gap is 0.654 eV as in Table III. Similar to the A-AFM LaMnO₃ experimental structure, spin splitting occurs along R- Γ -R' and R"- Γ symmetry lines and spin degeneracy is seen in the other \mathbf{k} -point region.

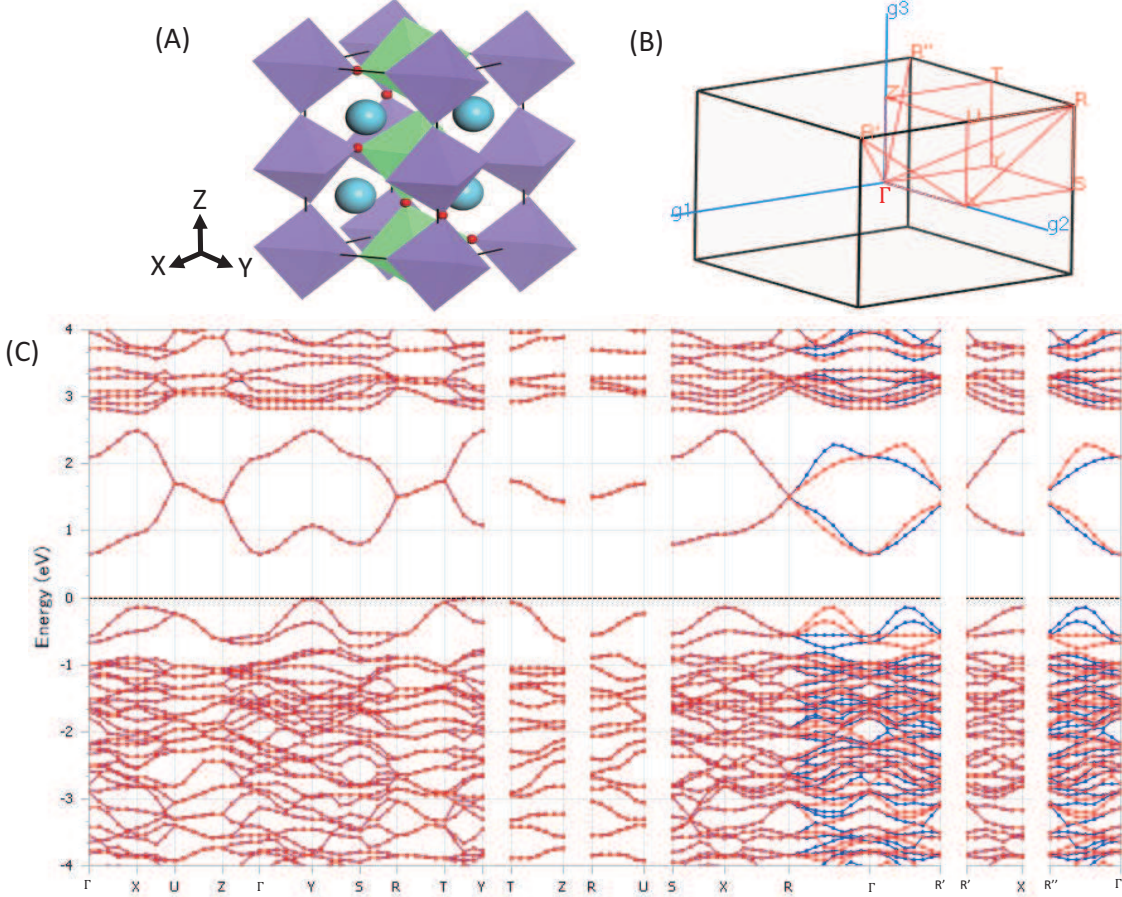


FIG. 5. (A) Unit cell and (B) Brillouin zone of the C-AFM LaMnO₃ experimental ORC structure. (C) Resulting band structure, in which red and blue lines denote up- and down-spin electron levels, respectively.

2. Spin degeneracy and splitting

This type of the structure has (A) a combination of 180 degree-rotation C_2 around y -axis and translation along [111] direction and (B) a combination of 180 degree-rotation C_2 around x -axis and translation along [110] direction as the exchange operations. The discussion for

the former combination (A) is the same as in the A-AFM LaMnO_3 experimental structure, and we find spin degeneracy on the Γ -X-U-Z- Γ -Y-S-R-T-Y, T-Z, R-U, S-X-R, and R'-X lines. On the other hand, the latter exchange operation (B), which does not exist in the A-AFM LaMnO_3 experimental structure, even cannot map the \mathbf{k} -points on the R- Γ -R' and Γ -R" lines onto themselves. Therefore, the \mathbf{k} -points on the R- Γ -R' and R"- Γ lines exhibit spin splitting.

In this case, the discussion about the \mathbf{k} -points on the Γ -R" and Γ -R lines is the same as the case of the A-AFM experimental structure because the same exchange operation (11) and the relationship (14) exist. Regarding the \mathbf{k} -points on the Γ -R and Γ -R' lines, a combination of 180 degree-rotation C_2 around x -axis, translation along [110] direction, and inversion, *i.e.*, a combination of (B) and inversion, can be used:

$$ITC_2^x \mathbf{k}(\Gamma\text{-R}) = \mathbf{k}(\Gamma\text{-R}'). \quad (16)$$

(Note that inversion itself is the symmetry operation in the space group.) Thus, the up-spin and down-spin energies on the Γ -R line exchange with those on the Γ -R" and Γ -R' lines.

E. G-type AFM experimental structure

1. LaMnO_3

The G-AFM LaMnO_3 experimental structure has a space-group symmetry $Pbnm$ with a simple orthorhombic lattice (ORC, see Fig. 6(A)), which is lowered to $P2_1/c$ by taking into account the spin configuration. The relaxed lattice constants are $a = 5.596 \text{ \AA}$, $b = 6.137 \text{ \AA}$, $c = 7.679 \text{ \AA}$ as shown in Table I. Figure 6(B) is the Brillouin zone of this structure. The band structure is shown in Fig. 6(C). There is a band gap of amount 1.278 eV as written in Table III. While the up- and down-spin energy levels are completely the same along the Γ -X-U-Z- Γ -Y-S-R-T-Y, T-Z, R-U, and S-X \mathbf{k} -lines, they are different along the X-R- Γ -R', R'-X, and R"- Γ lines.

2. Spin degeneracy and splitting

The exchange operations for this type of structure are (A) a combination of 180 degree-rotation C_2 around x -axis and translation along [110] direction, and (B) a combination of 180

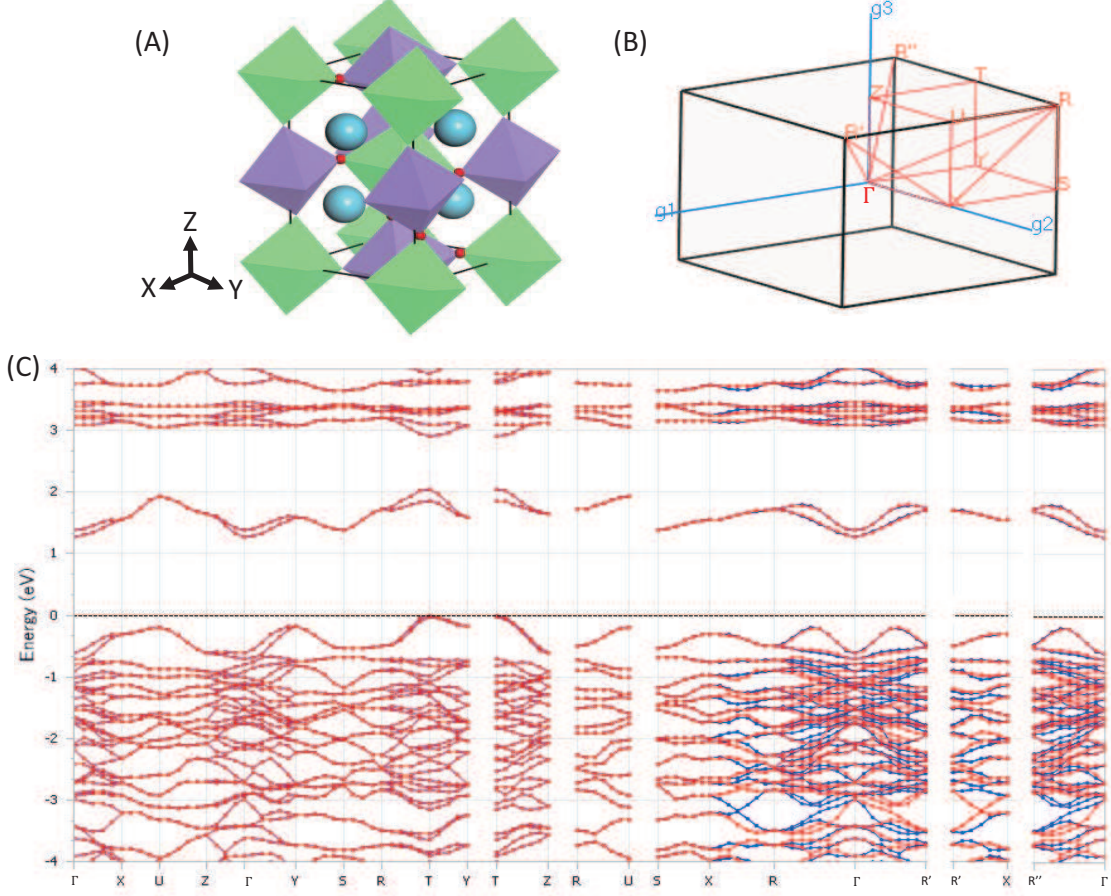


FIG. 6. (A) Unit cell and (B) Brillouin zone of the G-AFM LaMnO_3 experimental ORC structure. (C) Resulting band structure, in which red and blue lines denote up- and down-spin electron levels, respectively.

degree-rotation C_2 around z -axis and translation along [001] direction. By the combination (A),

$$TC_2^x V_{\downarrow} (TC_2^x)^{-1} = V_{\uparrow}. \quad (17)$$

Unchanged \mathbf{k} -points are on the Γ -X, Y-S, T-R, and Z-U lines:

$$TC_2^x \mathbf{k} = \mathbf{k} \quad \text{for the } \Gamma\text{-X line,} \quad (18)$$

$$TC_2^x \mathbf{k} = \mathbf{k} + \mathbf{G} \quad \text{for the Y-S, T-R, and Z-U lines.} \quad (19)$$

Due to the inversion symmetry, operation of I does not change the geometrical structure and the spin configuration. Therefore we can consider

$$ITC_2^x V_{\downarrow} (ITC_2^x)^{-1} = V_{\uparrow}, \quad (20)$$

and, under this operation, \mathbf{k} -points on Γ -X-U-Z- Γ and Y-S-R-T-Y lines do not change:

$$ITC_2^x \mathbf{k} = \mathbf{k} \quad \text{for the } \Gamma\text{-X-U-Z-}\Gamma \text{ line,} \quad (21)$$

$$ITC_2^x \mathbf{k} = \mathbf{k} + \mathbf{G} \quad \text{for the Y-S-R-T-Y line.} \quad (22)$$

Even if we use the combination (B), it changes \mathbf{k} -points on the X-R- Γ -R'-X and R"- Γ lines. Therefore, we see spin degeneracy for the \mathbf{k} -points on the Γ -X-U-Z- Γ -Y-S-R-T-Y, T-Z, R-U, and S-X-R lines and spin splitting on the X-R- Γ -R'-X and R"- Γ lines.

By using the exchange operation (20), we can obtain the relationship

$$ITC_2^x \mathbf{k} (\Gamma\text{-R}) = \mathbf{k} (\Gamma\text{-R}'), \quad (23)$$

$$ITC_2^z \mathbf{k} (\Gamma\text{-R}') = \mathbf{k} (\Gamma\text{-R}''). \quad (24)$$

Accordingly, the up-spin (down-spin) energy on the Γ -R' is the same as the down-spin (up-spin) energy on the Γ -R and Γ -R".

3. $LaCrO_3$

The G-AFM $LaCrO_3$ experimental structure has a space-group symmetry $Pbnm$ with a simple orthorhombic lattice (ORC, see Fig. 7(A)), which is lowered to $P2_1/c$ when the spin configuration is taken into account. Actually, this structure with the spin configuration is obtained experimentally¹⁸. After the geometrical optimization, the lattice constants are $a = 5.595 \text{ \AA}$, $b = 5.573 \text{ \AA}$, $c = 7.881 \text{ \AA}$ (experimental lattice constants are $a = 5.479 \text{ \AA}$, $b = 5.513 \text{ \AA}$, $c = 7.759 \text{ \AA}$) as shown in Table I. The Brillouin zone of this structure is shown in Figure 7(B), and the resulting band structure is shown in Fig. 7(C). According to our calculation, the band gap becomes 2.125 eV, which should be compared with the experimental values 2.8 eV¹⁵; see Table III.

The assignment of the spin splitting and degeneracy at each \mathbf{k} -point is exactly the same as the G-AFM experimental structure of $LaMnO_3$. Therefore, we see spin degeneracy for the \mathbf{k} -points on the Γ -X-U-Z- Γ -Y-S-R-T-Y, T-Z, R-U, and S-X-R lines and spin splitting on the X-R- Γ -R'-X and R"- Γ lines. For the results of A-type and C-type experimental structures of $LaCrO_3$, see SD.

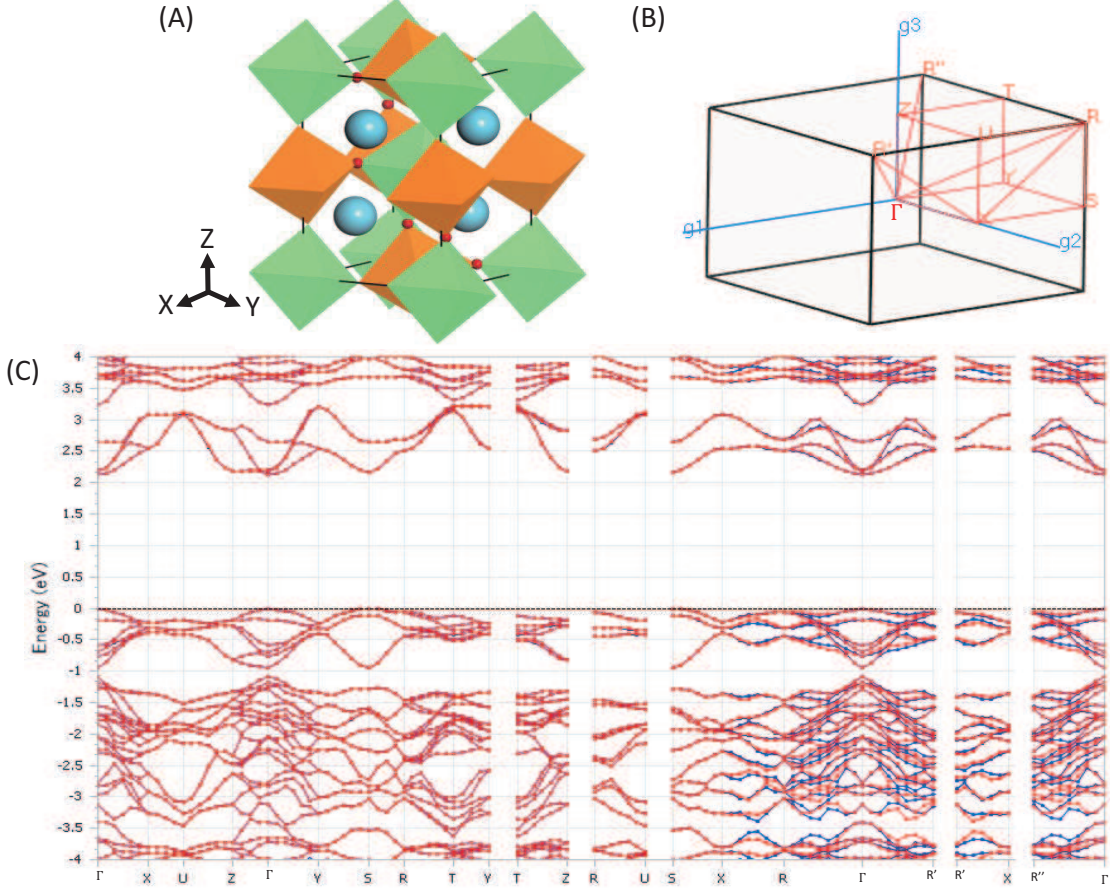


FIG. 7. (A) Unit cell of the G-AFM LaCrO₃ experimental ORC structure. Ocher- and green-coloured octahedra denote Cr atoms with up- and down-spin, respectively (the definition is also applied to SD). (B) Corresponding Brillouin zone and (C) resulting band structure, in which red and blue lines denote up- and down-spin electron levels, respectively.

4. *LaFeO₃*

The G-AFM LaFeO₃ experimental structure has a space-group symmetry *Pbnm* with a simple orthorhombic lattice (ORC, see Fig. 8(A)), which is lowered to *P2₁/c* when the spin configuration is taken into account. The spin configuration and the structure are the same as those reported experimentally^{18,19}. The lattice constants obtained by the geometrical optimization are $a = 5.611 \text{ \AA}$, $b = 5.689 \text{ \AA}$, $c = 7.970 \text{ \AA}$ (experimental lattice constants are $a = 5.553 \text{ \AA}$, $b = 5.563 \text{ \AA}$, $c = 7.857 \text{ \AA}$) as shown in Table I. The Brillouin zone and the resulting band structure are shown in Figures 8(B) and (C), respectively. The estimated band gap is 1.584 eV, which should be compared with the experimental values 2.1 eV¹³ and

1.2 eV¹⁹; see Table III.

The spin splitting and degenerate \mathbf{k} -points are exactly the same as the G-AFM experimental structures of LaMnO₃ and LaCrO₃. Therefore, we see spin degeneracy for the \mathbf{k} -points on the Γ -X-U-Z- Γ -Y-S-R-T-Y, T-Z, R-U, and S-X-R lines and spin splitting on the X-R- Γ -R'-X and R''- Γ lines. For the results of the A-type and C-type experimental structures of LaFeO₃, see SD.

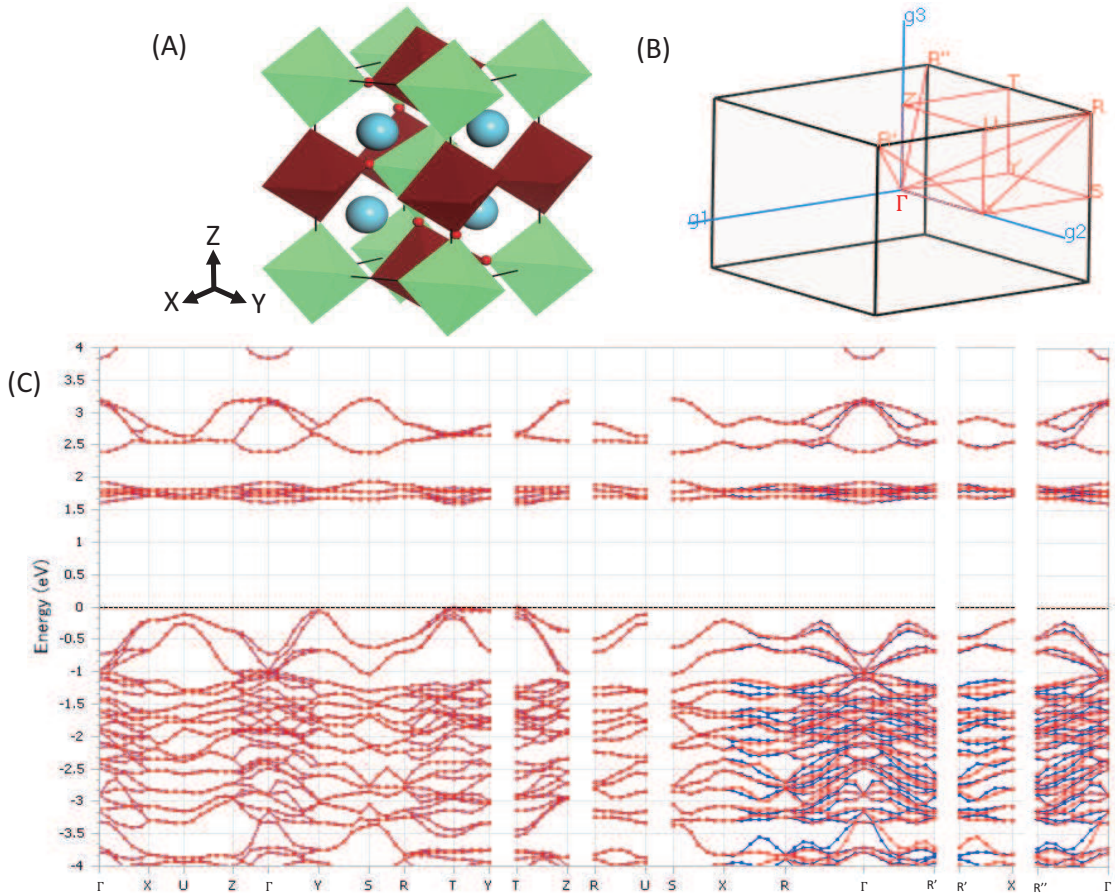


FIG. 8. (A) Unit cell of the G-AFM LaFeO₃ experimental ORC structure. Brown- and green-coloured octahedra denote Fe atoms with up- and down-spin, respectively (the definition is also applied to SD). (B) Corresponding Brillouin zone and (C) resulting band structure, in which red and blue lines denote up- and down-spin electron levels, respectively.

F. A brief comment on a preference for electrodes

We found that the resulting band structures of the most stable atomic and spin configurations of LaMO_3 ($\text{M} = \text{Cr, Mn, Fe}$) are very similar to each other and almost spin degenerate everywhere in the Brillouin zone, although a very small spin splitting appears in some \mathbf{k} -points. Therefore, after a carrier doping in these LaMO_3 materials, we expect that there is no preferable direction in the spin current and both up- and down-spin can equally contribute to the spin current in every direction. In order to discuss the OER and ORR activities of these materials, it is essential to consider the spin-dependent chemical reactions at surfaces as have been recently investigated by several authors^{4–6,31,32}. This is because every oxygen molecule associated with these reactions is spin triplet. Due to the local AFM ordering, spin directions are alternatively aligned also at surfaces. Therefore, to accelerate these reactions at the electrode surfaces, it would be also essential to evenly supply the spin-independent current in every direction in the bulk. In this sense, the almost spin-independent band structure in the bulk can be considered as a factor to enhance the OER and ORR reactivity of these materials. Indeed, these materials have recently attracted great interest in the OER and ORR applications^{4–6}. On the other hand, we should say that these materials are unfortunately not suitable for a device to separate the up-spin and down-spin currents in different directions, which could be possible if there was a significant spin dependence in the band structure.

V. CONCLUSION

We investigated the spin-dependent band structures for 15 types of antiferromagnetic (AFM) LaCrO_3 , LaMnO_3 , and LaFeO_3 by spin-polarized DFT with GGA+ U calculations. Geometry optimizations and band calculations were carried out to the 15 AFM LaCrO_3 , LaMnO_3 , and LaFeO_3 structures.

According to our calculation of the total energy, G-type magnetic configuration is the most stable for both LaFeO_3 and LaCrO_3 , which is consistent with the experimental results¹⁵. In the case of LaMnO_3 , A-type magnetic configuration is favored in the total energy comparison, which is also consistent with the experimental results^{12,14,15}. The results for the less stable cubic and JT-distorted structures of LaMnO_3 as well as the A- and C-AFM

experimental structures of LaCrO₃ and LaFeO₃ are given in SD.

From the resulting band structures, there is a very interesting difference between spin degeneracy and splitting depending on \mathbf{k} -points (*i.e.* electron or hole momentum) in the Brillouin zone. In the case of the A- and G-AFM LaMnO₃ ideal cubic perovskite and purely Jahn-Teller distorted structures, there is spin degeneracy in the whole Brillouin zone (see SD). In contrast, spin splitting can be seen in all \mathbf{k} -lines and \mathbf{k} -points for the C-AFM LaMnO₃ ideal cubic perovskite structure (see SD). Furthermore, there are both spin degenerate and splitting \mathbf{k} -points in the other LaMO₃ (M=Mn, Fe, and Cr) structures.

The difference between the spin splitting and degenerate \mathbf{k} -points in the present systems is also successfully explained by the very simple rule we found in the preceding paper³⁹: If a space-group symmetry operation R can map the effective (Kohn-Sham or more sophisticated self-energy-related) potential of an up-spin (down-spin) electron onto that of a down-spin (up-spin) electron, $RV_{\uparrow}R^{-1} = V_{\downarrow}$ ($RV_{\downarrow}R^{-1} = V_{\uparrow}$), and a certain wave vector \mathbf{k} is not changed under this operation, *i.e.* $R\mathbf{k} = \mathbf{k}$, then spin degeneracy can be seen at that \mathbf{k} -point in the band structure. Otherwise, for two different wave vectors \mathbf{k} and \mathbf{k}' which satisfy $R\mathbf{k} = \mathbf{k}'$ under the relationship $RV_{\sigma}R^{-1} = V_{-\sigma}$, the up-spin band energy at the \mathbf{k} -point and that of down-spin at \mathbf{k}' -point are the same, and *vice versa*. In the preceding paper³⁹, this rule was confirmed for the four phases of MnO₂ only. Now, we have succeeded in confirming the validity of this rule for variety of magnetic and structural types of AFM LaMnO₃, LaFeO₃, and LaCrO₃.

In the present study, we found that the band structures of the most stable atomic and spin configurations of LaMO₃ (M = Cr, Mn, Fe) are very similar to each other and almost spin degenerate everywhere in the Brillouin zone, although a very small spin splitting appears in some \mathbf{k} -points. Therefore, after a carrier doping in these LaMO₃ materials, we expect that there is no preference in the direction in the spin current and both up- and down-spins can equally contribute in every direction. This fact may favour the OER and ORR reactions of these electrodes, because they can evenly supply the spin-independent current in every direction. On the other hand, we should say that these materials are not suitable for a device to separate the up-spin and down-spin currents in different directions, which could be possible if there were a significant spin dependence in the band structure.

ACKNOWLEDGEMENTS

We are very grateful to Dr. Abhijit Chatterjee and Dr. Riichi Kuwahara at Dassault Systèmes BIOVIA for a lot of helpful discussions and support. This work was also supported in part by the Ministry of Education, Culture, Sports, Science and Technology (MEXT) Japan as a social and scientific priority issue (Creation of new functional devices and high-performance materials to support next-generation industries) to be tackled by using post-K computer for the use of the supercomputer facilities of the Supercomputer Centers at the Institute for Solid State Physics, the University of Tokyo, at Hokkaido University, and at IMR, Tohoku University (Project IDs. hp160072, hp160234, hp170268, and hp170190).

Supplementary Data (SD): Supplementary Data are available from “Public Full-text” at ResearchGate Web page:

<https://www.researchgate.net/publication/321416556>

- ¹ S. Mathews, R. Ramesh, T. Venkatesan, and J. Benedetto, *Science*, **276**, 238 (1997).
- ² M. K. Wu, J. R. Ashburn, C. J. Torng, P. H. Hor, R. L. Meng, L. Gao, Z. J. Huang, Y. Q. Wang, and C. W. Chu, *Phys. Rev. Lett.* **58**, 908 (1987).
- ³ Z. Guo, Y. Wan, M. Yang, J. Snaider, K. Zhu, L. Huang, *Science* **356**, 59 (2017).
- ⁴ J. Suntivich, K. J. May, H. A. Gasteiger, J. B. Goodenough and Y. Shao-Horn, *Science* **334**, 1383 (2011).
- ⁵ J. Suntivich, H. A. Gasteiger, N. Yabuuchi, H. Nakanishi, J. B. Goodenough and Y. Shao-Horn, *Nat. Chem.* **3**, 546 (2011).
- ⁶ K. A. Stoerzinger, M. Risch, J. Suntivich, W. M. Lu, J. Zhou, M. D. Biegalski, H. M. Christen, Ariando, T. Venkatesan and Y. Shao-Horn, *Energy Environ. Sci.* **6**, 1582 (2013).
- ⁷ S. A. Wolf, D. D. Awschalom, R. A. Buhrman, J. M. Daughton, S. von Molnar, M. L. Roukes, A. Y. Chtchelkanova, D. M. Treger, *Science* **294**, 1488 (2001).
- ⁸ S. Jin, T. H. Tiefel, M. McCormack, R. A. Fastnacht, R. Ramesh, and L. H. Chen, *Science* **264**, 413 (1994).
- ⁹ M. N. Baibich., J. M. Broto, A. Fert, F. Nguyen Van Dau, F. Petroff, P. Eitenne, G. Creuzet,

A. Friederich, and J. Chazelas, Phys. Rev. Lett. **61**, 2472 (1988).

¹⁰ J. M. D. Coey, M. Viret, S. von Molnar, Advances in Physics, **48**, 167 (1999).

¹¹ J. B. Goodenough, Phys. Rev. **100**, 564 (1955).

¹² J. B. A. A. Elemans, B. Van Laar, K. R. Van der Veen, and B. O. Loopstra, J. Solid State Chem. **3**, 238 (1971).

¹³ P. Norby, I. K. Andersen, E. K. Andersen, and N. Andersen, J. Solid State Chem. **119**, 191 (1995).

¹⁴ E. O. Wollan and W. C. Koehler, Phys. Rev. **100**, 545 (1955).

¹⁵ W. C. Koehler and E. O. Wollan, J. Phys. Chem. Solids **2**, 100 (1957).

¹⁶ K. Oikawa, T. Kamiyama, T. Hashimoto, Y. Shimojyo, and Y. Morii, J. Solid State Chem. **154**, 524 (2000).

¹⁷ S. Geller and E. A. Wood, Acta Cryst. **9**, 563 (1956).

¹⁸ R. Dogra, A. C. Junqueira, R. N. Saxena, A. W. Carbonari, J. Mestnik-Filho, and M. Moralles, Phys. Rev. B **63**, 224104 (2001).

¹⁹ G. L. Beausoleil II, P. Price, D. Thomsen, A. Punnoose, R. Ubic, S. Misture, and D. P. Butt, J. Am. Ceram. **97**, 228 (2014).

²⁰ I. Solovyev, N. Hamada, and K. Terakura, Phys. Rev. Lett. **76**, 4825 (1996).

²¹ Z.-Q. Yang, Z. Huang, L. Ye, and X. Xie, Phys. Rev. B **60**, 15674 (1999).

²² P. Ravindran, R. Vidya, H. Fjellvåg, A. Kjekshus, J. Crys. Growth **268**, 554 (2004).

²³ N. Soltani, S. M. Hosseini, and A. Kompany, Physica B **404**, 4007 (2009).

²⁴ T. Hashimoto, S. Ishibashi, and K. Terakura, Phys. Rev. B **82**, 045124 (2010).

²⁵ S. Gong and B.-G. Liu, Phys. Lett. A **375**, 1477 (2011).

²⁶ P. V. Sushko, L. Qiao, M. Bowden, T. Varga, G. J. Exarhos, F. K. Urban III, D. Barton, and S. A. Chambers, Phys. Rev. Lett. **110**, 077401 (2013).

²⁷ J. Hong, A. Stroppa, J. Íñiguez, S. Picozzi, and D. Vanderbilt, Phys. Rev. B **85**, 054417 (2012).

²⁸ J. He and C. Franchini, Phys. Rev. B **86**, 235117 (2012).

²⁹ M. D. Scafetta, A. M. Cordi, J. M. Rondinelli, and S. J. May, J. Phys.: Condens. Matter **26**, 505502 (2014).

³⁰ S. Javaid and M. J. Akhtar, J. Appl. Phys. **116**, 023704 (2014).

³¹ Y. Wang and H.-P. Cheng, J. Phys. Chem. C **117**, 2106 (2013).

³² Y.-L. Lee, M. J. Gadre, Y. Shao-Horn, and D. Morgan, Phys. Chem. Chem. Phys. **17**, 21643

(2015).

³³ Y.-J. Zhou, Z. Lü, B. Wei, Z.-B. Zhu, Q.-Y. Xie, Y.-Q. Li, and W.-H. Su, *Fuel Cells* **13**, 1040 (2013).

³⁴ Y.-J. Zhou, Z. Lü, B. Wei, S. Xu, D. Xu, and Z. Yang, *Ionics* **22**, 1153 (2016).

³⁵ I. W. Boateng, R. Tia, E. Adei, N. Y. Dzade, C. R. A. Catlow, and N. H. de Leeuw, *Phys. Chem. Chem. Phys.* **19**, 7399 (2017).

³⁶ T. Hotta, S. Yunoki, M. Nayr, and E. Dagotto, *Phys. Rev. B* **60**, R15009 (1999).

³⁷ C. Ederer, C. Lin, and A. J. Millis, Structural distortions and model Hamiltonian parameters: From LSDA to a tight-binding description of LaMnO₃ *Phys. Rev. B* **76**, 155105 (2007).

³⁸ R. Kováčik and C. Ederer, *Phys. Rev. B* **81**, 245108 (2010).

³⁹ Y. Noda, K. Ohno, S. Nakamura, *Phys. Chem. Chem. Phys.* **18**, 13294 (2016).

⁴⁰ D. M. Robinson, Y. B. Go, M. Mui, G. Gardner, Z. Zhang, D. Mastrogiovanni, E. Garfunkel, J. Li, M. Greenblatt, and G. C. Dismukes, *J. Am. Chem. Soc.* **135**, 3494 (2013).

⁴¹ M. D. Segall, P. J. D. Lindan, M. J. Probert, C. J. Pickard, P. J. Hasnip, S. J. Clark, and M. C. Payne, *J. Phys. Cond. Matter.* **14**, 2717 (2002).

⁴² CASTEP in Materials Studio, Biovia, Dassault Systèmes.

⁴³ S. J. Clark, M. D. Segall, C. J. Pickard, P. J. Hasnip, M. J. Probert, K. Refson, and M. C. Payne, *Z. Kristallographie* **220**, 567 (2005).

⁴⁴ D. Vanderbilt, *Phys. Rev. B* **41**, 7892 (1990).

⁴⁵ J. P. Perdew, K. Burke and M. Ernzerhof, *Phys. Rev. Lett.*, **77**, 3865 (1996).

⁴⁶ V. I. Anisimov, J. Zaanen, O. K. Andersen, *Phys. Rev. B* **44**, 943 (1991).

⁴⁷ V. I. Anisimov, J. Zaanen, *Phys. Rev. B* **52**, 5467 (1995).

⁴⁸ H. J. Monkhorst and J. D. Pack, *Phys. Rev. B* **13**, 5188 (1976).

⁴⁹ K. Maiti and D. D. Sarma, *Phys. Rev. B* **54**, 7816 (1996).

⁵⁰ R. Mahendiran, A. K. Raychaudhuri, A. Chainani, D. D. Sarma, and S. B. Roy, *Appl. Phys. Lett.* **66**, 233 (1995).

⁵¹ J. H. Jung, K. H. Kim, D. J. Eom, and T. W. Noh, E. J. Choi, J. Yu, Y. S. Kwon, and Y. Chung, *Phys. Rev. B* **55**, 15489 (1997).

⁵² T. Arima, Y. Tokura, and J. B. Torrance, *Phys. Rev. B* **48**, 17006 (1993).

⁵³ M. B. Bellakki, B. J. Kelly, and V. Manivannan, *J. Alloys Compd.* **489**, 64 (2010).

⁵⁴ F. L. Hirshfeld, *Theoret. Chim. Acta (Berl.)* **44**, 129- (1977).

⁵⁵ J. Kanamori, J. Phys. Chem. Solids **10**, 87 (1959).

⁵⁶ P. A. Cox, *Transition Metal Oxides: An Introduction to Their Electronic Structure and Properties*, Clarendon Press, Oxford, 1995.

⁵⁷ T. Okugawa, K. Ohno, Y. Noda, and S. Nakamura, J. Phys.: Condens. Matter **30**, 075502 (2018).